JOURNAL OF AIRCRAFT
Vol. 43, No. 2, March–April 2006

# New Hybrid Method for Predicting the Flowfields of Helicopter Rotors

Qi-Jun Zhao* and Guo-Hua Xu†
*Nanjing University of Aeronautics and Astronautics, Nanjing 210016, People's Republic of China*
and
Jing-Gen Zhao‡
*Georgia Institute of Technology, Atlanta, Georgia 30332*

**Based on a Navier–Stokes/full potential/free wake solver, a new hybrid method was developed for efficient predictions of the three-dimensional viscous flowfield of a helicopter rotor under both hover and forward flight conditions. The developed flow solver was composed of three modules: 1) a compressible Navier–Stokes analysis to model the viscous flow and near wake about the blade, 2) a compressible potential flow analysis to model the inviscid isentropic potential flow region far away from the rotor, and 3) a free wake model to account for tip vortex effects once the tip vortex leaves the viscous flow region and enters the potential flow region. In this hybrid method, a moving embedded grid methodology was adopted that accounts for rigid blade motions in rotation, flapping, and pitching. A dual-time method was employed to fulfill the calculation of the unsteady flowfields of helicopter rotors, and a third-order upwind scheme (MUSCL) and flux-difference splitting scheme without introducing artificial viscosity were used to calculate the flux. To search suitable donor elements in embedded grids to pass information between the viscous flow and potential flow zones, a new searching scheme was implemented. The sectional pressure distributions of a UH-60A helicopter rotor and an AH-1G model rotor in hover and forward flight, with and without the wake model, were calculated, and the developed hybrid model was validated by comparing with available experimental data. The simulated steady and unsteady lifting results of a model rotor with three different blade-tip planforms demonstrate the benefits of the curvilinear swept tip and constant swept tip in suppressing supercritical flows.**

## Nomenclature

| | | |
|---|---|---|
| $A_1$ | = | lateral cyclic pitch angle |
| $a_0$ | = | cone angle |
| $a_{1s}$ | = | longitudinal tip-path-plane tilt angle |
| $B_1$ | = | longitudinal cyclic pitch angle |
| $b_{1s}$ | = | lateral tip-path-plane tilt angle |
| $C_L$ | = | section lift coefficient |
| $C_P$ | = | pressure coefficient |
| $\boldsymbol{F}_v$ | = | viscid flux |
| $\boldsymbol{F}_1$ | = | inviscid flux |
| $L$ | = | spanwise lift distribution |
| $M_{\text{tip}}$ | = | tip Mach number |
| $p$ | = | pressure |
| $\boldsymbol{Q}$ | = | convective inviscid fluxes |
| $\boldsymbol{Q}^v$ | = | convective viscid fluxes |
| $\boldsymbol{q} = (u, v, w)$ | = | velocity vector in Cartesian coordinate system |
| $\boldsymbol{q}_b = (u_b, v_b, w_b)$ | = | grid velocity vector in Cartesian coordinate system |
| $\boldsymbol{q}_\infty$ | = | freestream velocity |
| $\boldsymbol{R}(\psi, \zeta)$ | = | location vector of a collocation point on vortex filament |
| $r/R$ | = | radial blade station nondimensionalized by rotor radius |
| $S$ | = | surface of the control cell |
| $T$ | = | absolute temperature |
| $t$ | = | physical time |
| $V$ | = | control cell volume |
| $\boldsymbol{W}$ | = | vector of conserved flow variables |
| $x, y, z$ | = | Cartesian coordinate system |
| $\beta(t)$ | = | flapping angle |
| $\Gamma$ | = | circulation of vortex |
| $\Delta_+$ | = | forward difference operator |
| $\Delta_-$ | = | backward difference operator |
| $\zeta$ | = | wake age |
| $\theta(t)$ | = | blade pitch angle |
| $\theta_0$ | = | collective pitch angle |
| $\mu$ | = | advance ratio |
| $\rho$ | = | air density |
| $\tau$ | = | pseudo time |
| $\phi$ | = | velocity potential |
| $\psi(t)$ | = | azimuth angle |
| $\Omega$ | = | rotor rotational speed |
| $\omega_R$ | = | relaxation factor |

*Subscripts*

| | | |
|---|---|---|
| $i, j, k$ | = | grid indices |
| $\boldsymbol{n}$ | = | local surface normal vector |
| $\infty$ | = | undisturbed flow |

## I. Introduction

TO design an efficient and quiet helicopter, it is imperative to accurately and efficiently analyze complex rotor flowfield. However, in spite of significant advances in computational techniques[1] and computer hardwares during the past several decades, an accurate and efficient numerical simulation of rotor wake effects is still one of the most challenging problems in the rotorcraft industry. A key problem is the false dissipation of the wake vorticity due to truncation errors and artificial viscosity presented in numerical algorithms. Also, high CPU time consumption makes computational fluid dynamics analysis difficult to use in routine analysis.

Received 30 November 2004; revision received 17 March 2005; accepted for publication 20 March 2005. 

*Ph.D. Student, P.O. Box 331, National Key Laboratory of Rotorcraft Aeromechanics; zhaoqijun@nuaa.edu.cn.

†Professor, P.O. Box 331, National Key Laboratory of Rotorcraft Aeromechanics; ghxu@nuaa.edu.cn.

‡Ph.D. Student.

The existing finite difference methodologies in rotorcraft aerodynamics can be divided into two categories, depending on how they treat the wake effect. One type of code is the so-called Eulerian method, which tries to capture the rotor vortex wake entirely from first principles. Although it eliminates the need for external wake models, it requires significant computer resources. In addition, the tip vortex cannot be resolved for long distances after it leaves the blade, due to the high level of numerical viscosity presented in these schemes, particularly on coarse grids far away from the rotor disk. Some algorithms, such as grid refinement,[2] unstructured grids,[3] and high-order-accuracy differencing,[4] have appeared in the literature for high-order vortex modeling, but it seems that none of these algorithms have yet been demonstrated to be able to capture the vortex wake behind a rotor with sufficient resolution.

The other type of code is based on hybrid methods, which combine the Eulerian approach with a free or rigid wake analysis. For example, a hybrid Navier–Stokes/full potential/free wake method was proposed by Sankar and colleagues,[5,6] where a Lagrangian approach was used to track the vortex filaments once they left the Navier–Stokes (NS) zone and entered the potential flow zone. The method not only reduced the computation time, but also improved the simulation accuracy for the rotor wake. However, it should be noted that there is an exact one-to-one matching relation between the potential flow and viscous zones at zone interfaces in this method; this will increase the difficulty of generating the grids for the two zones, especially when the blade flapping and pitching motions are considered, and less information is passed between the zones. Additionally, the model used in their studies only considers the tip vortex, and the inboard vortex is neglected.

In the present investigation, a new hybrid method, which is composed of a Navier–Stokes solver, a full-potential solver, and a free-wake analysis, based on a moving embedded grid methodology and a high-order upwind algorithm, was developed to simulate the near flowfield of helicopter rotors in hover and forward flight. To effectively reduce the false dissipation of the rotor wake vorticity presented in Jameson's second-order cell-centered finite volume approach, a third-order monotone upwind–centered scheme for conservation laws[7] (MUSCL) and flux-difference splitting scheme without the introduction of artificial viscosity were used. All other regions where viscous effects are minor were modeled using a potential flow solver and a wake model. A multifilament free wake analysis was incorporated to account for the far wake effects.

The moving embedded grid methodology was used to account for actual blade rotational motions, and flapping and pitching motions. The methodology used can avoid building a one-to-one matching relation between the potential flow zone and the viscous flow zone, and can thus pass more information between the zones. To efficiently identify the donor elements in the moving embedded grids for interpolations between the two zones, the present algorithm adopted a new searching approach, the pseudo-searching Scheme of donor elements (PSSDE), which was shown to be more effective and robust in searching the corresponding donor elements and getting the interpolated data.

## II. Moving-Embedded Grid System

### A. Embedded Grid Generation

The embedded grids used in this study (as shown in Fig. 1), which account for the rigid blade flapping and pitching motion, consist of the cylindrical O-H background grids and the body-fitted and body-orthogonal C-H grids around the blade. The former set of grids consists of 41 points in the radial direction, 71 points in the axial direction, and 72 points in the circumferential direction. The latter set of grids, which was generated using an improved geometry algorithm by the authors[8] together with the Poisson equations, has 65 points in the spanwise direction, 33 points in the normal direction, and 193 points in the chordwise direction. Because several variables in the governing equations vary very fast in the blade tip region, the grids in this region must be refined. For example, the grid size around the azimuthal, radial, and axial directions in the O-H background grid near the blade tip should be reduced, and the grid size around the radial direction in the C-H grids should be reduced also.

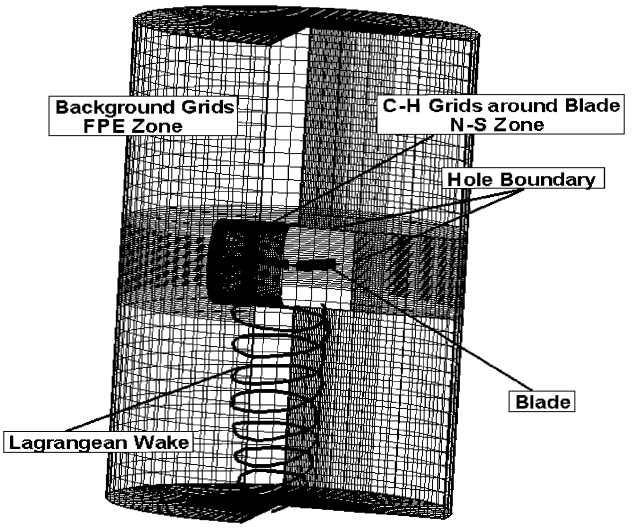


**Fig. 1 Overall schematic of an embedded grid system for the hybrid method solver.**

The whole flowfield is divided into two zones. The first zone covers a small region around each blade, which is shown in Fig. 1. In this zone the viscous effect is modeled using a Navier–Stokes solver. The second zone includes the inviscid "potential flow" region away from the blade, and a free wake is embedded into the zone to capture the rotor wake effect.

### B. Rigid Blade Motion

In the current study, the rigid blade flapping motion, pitching motion, and rotational motion are accounted for as follows:

$$\beta(t) = a_0 - a_{1s}\cos\psi(t) - b_{1s}\sin\psi(t)$$

$$\theta(t) = \theta_0 - A_1\cos\psi(t) - B_1\sin\psi(t), \qquad \psi(t) = \Omega t \quad (1)$$

The position of a typical point on the blade, $\boldsymbol{r}(x, y, z, t)$, at any physical time instant can be related to its initial position, $\boldsymbol{r}^0(x, y, z, 0)$, through the coordinate system transformation

$$\boldsymbol{r} = R_{\psi(t)}R_{\beta(t)}R_{\theta(t)}\boldsymbol{r}^0 = T\boldsymbol{r}^0 \quad (2)$$

where $T$ is a transformation matrix and consists of three subsequent rotations, $R_{\psi(t)}$ (rotation direction), $R_{\beta(t)}$ (flapping direction), and $R_{\theta(t)}$ (feathering direction).

Without the rigid blade motion assumption, the grid motion will incur additional elastic rotations in pitching and elastic bending deformations, which are not accounted for in the present work for simplicity.

## III. Mathematical Formulations

### A. Viscous Zone

The NS equations over the moving-embedded grids are formulated in an inertial coordinate system, which avoids the addition of a source term to account for the rotational motion of blades. The governing equations can be written in finite volume form as

$$\frac{\mathrm{d}}{\mathrm{d}t}\iiint_V \boldsymbol{W}\,\mathrm{d}v + \iint_S \boldsymbol{F}_1\cdot\boldsymbol{n}\,\mathrm{d}S - \iint_S \boldsymbol{F}_v\cdot\boldsymbol{n}\,\mathrm{d}S = 0 \quad (3)$$

#### 1. *Spatial Discretization in Finite-Volume Formulation*

The finite-volume method was employed to calculate the flowfield around helicopter rotors. The numerical fluxes on the connected surface was constructed in two stages: 1) a high-order interpolation was used to determine the state variables on each side of a cell face, and 2) these interpolated variables were used as initial data for an approximate Riemann solver to obtain numerical fluxes.

Third-order monotone upwind interpolation (a MUSCL scheme) was used to determine the state variables on each side of a cell face. Because the scheme is dissipative in essence and high-order accurate, it can effectively reduce the false dissipation of the rotor wake vorticity without introducing artificial viscosity, which is needed if a second-order cell-centered difference approach[9] is used.

To reduce the computation costs in the exact solution of the Riemann problem, Roe's approximate Riemann solver[10] was employed in the present work. Roe's method is widely used due to its high accuracy for boundary layers and good resolution to shocks. The flux-difference splitting schemes evaluate the convective fluxes at a face of the control volume from the left and right states by solving the Riemann (shock) problem. The numerical convective fluxes can be expressed as

$$(\boldsymbol{Q})_{i+\frac{1}{2}} = \tfrac{1}{2}\left[\boldsymbol{Q}(\boldsymbol{W}_R) + \boldsymbol{Q}(\boldsymbol{W}_L) - |\tilde{A}_{\mathrm{Roe}}|_{i+\frac{1}{2}}(\boldsymbol{W}_R - \boldsymbol{W}_L)\right] \quad (4)$$

In Eq. (4), $\tilde{A}_{\mathrm{Roe}}$ denotes the Roe-averaged Jacobian matrix, and subscripts $L$ and $R$ denote the states at the left and right surfaces of a control volume, respectively. The flux-difference splitting schemes consider not only the direction of wave (information) propagation, but also the waves themselves.

Linear interpolation formulas such as the MUSCL scheme are inadequate because they can cause oscillations in the presence of discontinuities. Monotonicity principles are invoked at the interpolation stage to suppress the artificially introduced oscillations, and the modified interpolation formulas can be written as

$$U_R = U_{i+1} - \tfrac{1}{2}\Psi_R\Delta_+ U_{i+1}, \qquad U_L = U_i + \tfrac{1}{2}\Psi_L\Delta_- U_i$$

$$\Psi_{L/R} = \left(\tfrac{2}{3}r_{L/R} + \tfrac{1}{3}\right)\Phi_{L/R} \quad (5)$$

where $\Psi_{L/R}$ is a limiter function, and $r_L = (\Delta_+/\Delta_-)U_i$, $r_R = (\Delta_-/\Delta_+)U_{i+1}$, and $\Phi(r) = 3r/(2r^2 - r + 2)$.

To prevent the occurrence of an unphysical expansion shock in Roe's approximate Riemann solver, for which $(\boldsymbol{Q}_C)_R = (\boldsymbol{Q}_C)_L$ but $\boldsymbol{W}_R \neq \boldsymbol{W}_L$, the modulus of eigenvalues can be modified using Harten's entropy correction.[11]

The algebraic turbulence model of the Cebeci–Smith balance model, which consists of a blend of inner and outer eddy viscosities, was employed to calculate the turbulence flow viscosity coefficient $\mu_t$, and the laminar flow viscosity coefficient $\mu_l$ is obtained using the Sutherland law. Then the two viscosity coefficients are added together to obtain the global viscosity coefficient for viscous flow.

*2. Time Discretization in Finite-Volume Formulation*

A dual time-stepping approach was adopted in the present study for the prediction of the three-dimensional flowfield around helicopter rotors under both hover and forward flight conditions. In this approach, the solution is marched forward in pseudo-time to steady state through an explicit multistage scheme at each physical time level. During the marching in pseudo-time, the physical time is fixed, which permits the acceleration techniques of steady flow calculations such as a local time-stepping scheme and an implicit residual smoothing method to be used. Therefore, Eq. (3) can be replaced by

$$\frac{\mathrm{d}}{\mathrm{d}\tau}(\boldsymbol{W}^{m+1}) = -\boldsymbol{R}^*(\boldsymbol{W}^{m+1})$$

$$\boldsymbol{R}^*(\boldsymbol{W}^{m+1}) = \frac{\mathrm{d}}{\mathrm{d}t}(\boldsymbol{W}^{m+1}) + \frac{1}{V}[Q(\boldsymbol{W}^{m+1}) - Q(\boldsymbol{W}^{m+1})] \quad (6)$$

with

$$\frac{\mathrm{d}}{\mathrm{d}t}\boldsymbol{W}^{m+1} = \frac{3\boldsymbol{W}^{m+1} - 4\boldsymbol{W}^m + \boldsymbol{W}^{m-1}}{2\Delta t}$$

In Eq. (6), $\Delta t = 2\pi/\Omega IB$ is the physical azimuthal step, and $IB$ is the number of grid points along the circumferential direction in background grids.

The explicit five-stage Runge–Kutta scheme is used to integrate Eq. (6). The pseudo-time step is restricted by stability considerations. For each cell the allowable pseudo-time step is chosen using

$$\Delta\tau_{i,j,k} = \min\left[\frac{2}{3}\Delta t, \frac{\mathrm{CFL}\cdot V_{i,j,k}}{\lambda_i + \lambda_j + \lambda_k}\right] \quad (7)$$

where $\lambda_i$, $\lambda_j$ and $\lambda_k$ are the spectral radii of the Jacobian matrices of flux vectors in the $i$, $j$, and $k$ directions, respectively, and CFL represents the Courant number.

At each new global physical time, which is related to blade position, the initial guess for $\boldsymbol{W}^{m+1}$ is given by a three-point backward-difference approximation of the time in Eq. (6) as follows:

$$(\boldsymbol{W}^*)^0 = \boldsymbol{W}^m + (3\boldsymbol{W}^m - 4\boldsymbol{W}^{m-1} + W^{m-2})/2 \quad (8)$$

### B. Potential Flow Zone

A potential flow solver is used to solve the continuity equation

$$\frac{\mathrm{d}}{\mathrm{d}t}\iiint_V \rho\,\mathrm{d}v + \iint_S \rho(\boldsymbol{q} - \boldsymbol{q}_b)\cdot\boldsymbol{n}\,\mathrm{d}S = 0 \quad (9)$$

where the flow velocity $q$ is composed of three components: the freestream velocity $\boldsymbol{q}_\infty$, the disturbance potential velocity $\nabla\phi$, and the induced velocity $\boldsymbol{q}^v$ induced by the free wake.

A three-dimensional unsteady compressible potential flow solver that uses a rotating difference method and a SLOR method to solve the difference equation is used to solve Eq. (9). Although the potential flow solver can capture the embedded weak shock waves and model the convection of acoustic waves in a time-accurate manner, it cannot capture the vortex wake effect. Therefore, a free wake model was added into the zone to model the effect of the rotor wake.

### C. Free Wake Model

A full span free wake model[12] developed at the Nanjing University of Aeronautics and Astronautics is employed to account for rotor wake effects in the potential flow zone. The model used in this study considers not only the tip vortex, but also the inboard vortex from the blade. In this study, three inboard vortex filaments are included in the full wake free-wake model. The helical vortices are modeled by a connected series of straight-line elements with azimuth increment of 5 deg. An undistorted classical helical wake (up to 10 revolutions) is used as an initial guess to start the solution process.

The governing equation[13] describing the motion of a vortex filament can be expressed as

$$\frac{\mathrm{d}\boldsymbol{R}(\psi,\zeta)}{\mathrm{d}t} = \Omega\left(\frac{\partial\boldsymbol{R}(\psi,\zeta)}{\partial\zeta} + \frac{\partial\boldsymbol{R}(\psi,\zeta)}{\partial\psi}\right)$$

$$= \boldsymbol{q}_\infty + \boldsymbol{q}^v(\boldsymbol{R}(\psi,\zeta)) \quad (10)$$

In the present analysis, a five-point difference scheme[13] with equal difference steps, that is, $\Delta\psi = \Delta\zeta$, was used. A prediction–correction–relaxation scheme improved over Ref. 12, which has better stabilities, is presented to solve the differential equation with initial and boundary conditions.

*Prediction:*

$$\boldsymbol{R}'(\psi_k,\zeta_j) = \boldsymbol{R}'(\psi_{k-1},\zeta_{j-1}) + (\Delta\psi/\Omega)$$
$$\times\left\{\boldsymbol{q}_\infty + \tfrac{1}{4}\left[(\boldsymbol{q}^v)^{n-1}(\psi_k,\zeta_j) + (\boldsymbol{q}^v)^{n-1}(\psi_k,\zeta_{j-1})\right.\right.$$
$$\left.\left. + (\boldsymbol{q}^v)^{n-1}(\psi_{k-1},\zeta_j) + (\boldsymbol{q}^v)^{n-1}(\psi_{k-1},\zeta_{j-1})\right]\right\} \quad (11)$$

*Correction:*

$$\boldsymbol{R}^n(\psi_k,\zeta_j) = \boldsymbol{R}^n(\psi_{k-1},\zeta_{j-1}) + (\Delta\psi/\Omega)$$
$$\times\left\{q_\infty + \tfrac{1}{4}\left[(\boldsymbol{q}^v)'(\psi_k,\zeta_j) + (\boldsymbol{q}^v)'(\psi_k,\zeta_{j-1})\right.\right.$$
$$\left.\left. + (\boldsymbol{q}^v)'(\psi_{k-1},\zeta_j) + (\boldsymbol{q}^v)'(\psi_{k-1},\zeta_{j-1})\right]\right\} \quad (12)$$

*Relaxation:*

$$\boldsymbol{R}^n(\psi_k, \zeta_j) = \omega_R \boldsymbol{R}^n(\psi_k, \zeta_j) + (1 - \omega_R)\boldsymbol{R}^{n-1}(\psi_k, \zeta_j) \tag{13}$$

where $\omega_R$ is the relaxation factor, and a value of 0.6–0.8 is suggested for the solution. In the current application, $\omega_R = 0.7$.

A vortex core model[14] based upon experimental results on rotor tip vortices was used in the current study. Given the vorticity strength and the wake geometry, the induced velocity due to the free wake system can be evaluated by the Biot–Savart law. Then the calculated induced velocities are included in the potential flow analysis [Eq. (9)]. Through interpolation, the Navier–Stokes nodes will feel the effects of the rotor wake–induced velocity field.

### D. Information Communication Among the Full-Potential, Navier–Stokes, and Free Wake Zones

*1. Passing Information from the Navier–Stokes Zone to the Full-Potential Zone*

To allow the three types of waves (acoustic, vorticity, and entropy waves) to propagate out from the Navier–Stokes zone to the full-potential zone without false reflections, the embedded region between the two zones should be carefully handled.

The initial portions of the vortices after their generation on the blade are solved inside the Navier–Stokes zone. On the full-potential inner boundary, they are converted into vortex filaments made up of wake markers.

The circulation $\Gamma$ of the vortex is defined as the line integral of velocity $\boldsymbol{q}$ around any closed curve $C$, which is the boundary of any surface $S$.

$$\Gamma = \oint \boldsymbol{q} \cdot \mathrm{d}\boldsymbol{l} \tag{14}$$

The circulation can be related to the vorticity on the surface $S$ with the use of Stokes' theorem as

$$\int_s \nabla \times \boldsymbol{q} \cdot \mathrm{d}S = \oint_C \boldsymbol{q} \cdot \mathrm{d}\boldsymbol{l} \tag{15}$$

To calculate the flux crossing the inner boundary of the full-potential zone, that is, $\rho q_n \Delta S$, the potential flow solver requires the normal velocity $q_n$ and the density $\rho$, which can be computed by interpolation.

*2. Passing Information from the Full-Potential Zone to the Navier–Stokes Zone*

On the boundaries between the full-potential zone and the Navier–Stokes one, the flow properties for the Navier–Stokes equations are computed directly from the full-potential domain. The velocity components are computed by adding the potential velocity, freestream velocity, and wake-induced velocity, the temperature $T$ is obtained through the energy equation, and the density $\rho$ and pressure $p$ are solved by using the isentropic law:

$$u = \boldsymbol{q}_{\infty x} + \phi_x + \boldsymbol{q}^v \cdot \boldsymbol{i}, \qquad v = \boldsymbol{q}_{\infty y} + \phi_y + \boldsymbol{q}^v \cdot \boldsymbol{j}$$
$$w = \boldsymbol{q}_{\infty z} + \phi_z + \boldsymbol{q}^v \cdot \boldsymbol{k} \tag{16}$$

where the derivatives $\phi_x$, $\phi_y$, and $\phi_z$ are calculated by the difference method.

### E. Other Boundary Conditions

Since the Navier–Stokes equation automatically considers viscosity, the no-slip boundary condition is employed on the blade surface. The normal derivatives are equal to zero, namely, $\partial T/\partial n = 0$ for an adiabatic wall and $\partial p/\partial n = 0$, for the thermodynamic and dynamic boundary conditions.

In the present approach, the far field is usually located one or more rotor diameters away from the rotor disk. As a result, the reflection of acoustic waves in the far field is not a major consideration, and the approach sets the disturbance potential $\phi$ to zero on the far boundaries.

### F. Searching Donor Elements

To get the interpolation information from the Navier–Stokes zone for both the full-potential and free-wake zones, two issues should be handled carefully: 1) identifying the hole boundary and hole points; 2) searching suitable donor elements. A new searching algorithm, namely the PSSDE, was adopted in the present study, which consists of the following two steps.

*Step 1:* Generate the inverse map $F_M$ over the grid $F$ and keep the relative position between them, in order to search for a suitable donor element bounding any point $P$. Then identify the element in $F$ that bounds any point of $F_M$, and predict the reference position of the point in the element.

*Step 2:* First, identify the donor element in $F_M$ that bounds the point $P$, and predict the reference position of the point. Because the donor element is among $F_M$ instead of $F$, the method is called the pseudo-searching scheme of donor elements (PSSDE). Second, obtain the interpolated data for the four (eight for three dimensions) vertices of a pseudo-donor element bounding point $P$ from the known points, and subsequently get the communication for the point $P$ by bilinear interpolation (trilinear interpolation for three dimensions).

In the searching process, only one piece of the two-dimensional inverse map over structured C-grids around the blade airfoil is needed and the generated inverse map is used to get the interpolated data for the hole of background grids from rotor grids. In addition, the identification of the corresponding donor elements for the outer boundary of the Navier–Stokes zone and the markers of the free wake in the background grids can be analytically performed. The analytical formula are given as follows:

$$I = \begin{cases} IB + \mathrm{int}(\arctan(y/x)/\Delta\psi), & x > 0,\ y < 0 \\ IB/2 + \mathrm{int}(\arctan(y/x)/\Delta\psi), & x < 0,\ y > 0 \\ I + \mathrm{int}(\arctan(y/x)/\Delta\psi), & x > 0,\ y > 0 \\ IB/2 + 1 + \mathrm{int}(\arctan(y/x)/\Delta\psi), & x < 0,\ y < 0 \end{cases}$$

$$J = \mathrm{int}\left(\sqrt{x^2 + y^2}\big/\Delta r\right), \qquad K = \mathrm{int}(z/\Delta z) \tag{17}$$

where $(I, J, K)$ represent the suitable donor elements, and $\Delta\psi$, $\Delta r$, and $\Delta z$ are the grid intervals in azimuthal, radial, and axial directions, respectively, in the background grid.

## IV. Flow Chart of the Hybrid Solver

To calculate the complicated rotor flowfield, the moving embedded grids generation model, the dual-time methodology employing an explicit multistage scheme, the cell-centered finite-volume method, the full-potential solver and the free-wake analysis, which are described in previous sections, are coupled together, and the iterative procedure is schematically shown in Fig. 2.

In the flow chart, for the calculations in the forward flight condition, there are four convergence criterions, among which two are for the conservation variables, one is for the full-potential solver, and the last is for the free wake geometry. The first one was used in pseudo-time; the second one is used to judge the convergence of the variables at the same points on the rotor blade between two consecutive rotor revolutions in the global physical time. Generally, the above algorithm converges quickly and the periodic solutions can be obtained within three rotor revolutions, and a value of $10^{-6}$ for air density in the residual is used as the threshold of the above three convergence cases. For the calculation in hover, the second convergence criterion is not needed.

The convergence criterion for free wake geometry is based on a modified root-mean-square (rms) residual in the wake geometry between two successive iterations, and the rms is defined in the following form:

$$\mathrm{rms} = \sqrt{\frac{\sum_k^{N_a}\sum_j^{N_c}\sum_i^{N_s}\left[\boldsymbol{r}_w^n(i,j,k) - \boldsymbol{r}_w^{n-1}(i,j,k)\right]^2}{N_s N_c N_a}} < \varepsilon \tag{18}$$

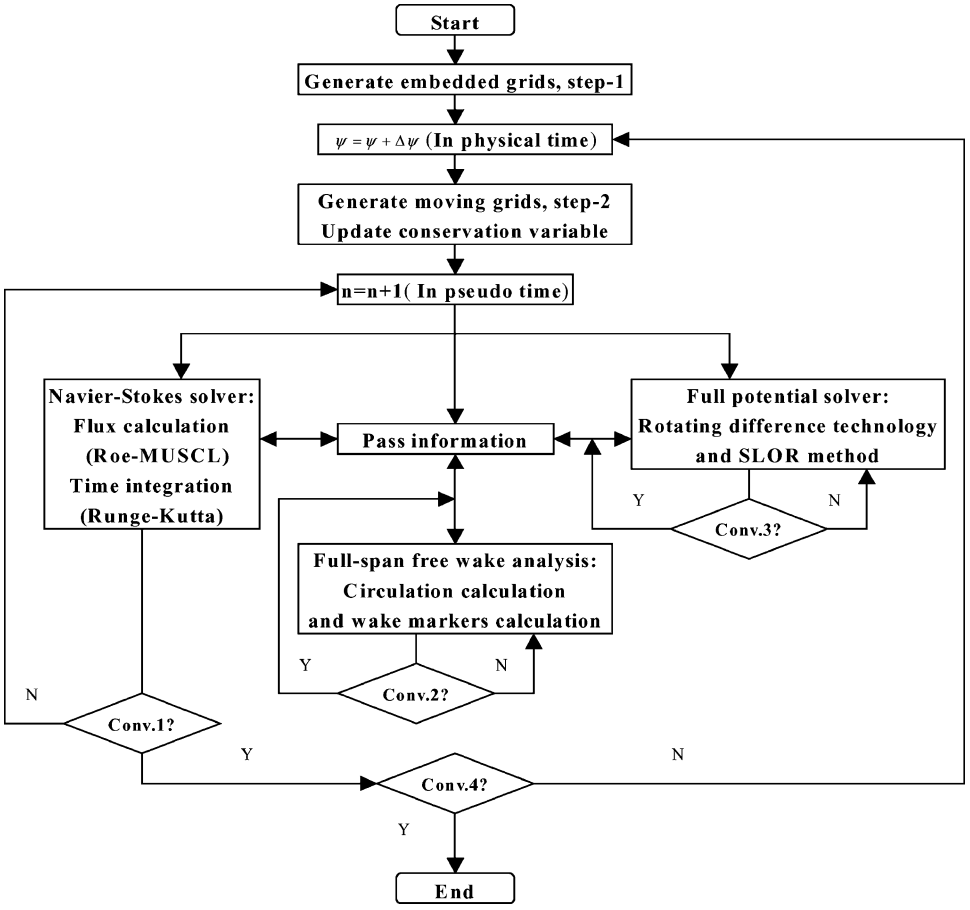


**Fig. 2 Flow chart of the hybrid method solver.**

where $r_w$ denotes the location vector of a collocation point on vortex filament, $\varepsilon$ represents the convergence threshold, $N_s$ is the number of trailed vortex filaments, $N_c$ is the total number of collocation points used to describe each of trailed vortex filaments, and $N_a$ is the number of blade azimuth steps for each rotor revolution. The convergence of wake geometries calculated by the present prediction–correction–relaxation scheme can be achieved after the rms value drops below $10^{-3}$.

## V. Results and Discussions

The new hybrid analysis proposed in this work is validated by comparing the simulation results for a four-bladed UH-60A helicopter rotor and a two-bladed Caradonna and Tung model rotor in hover, and a two-bladed AH-1G rotor and H-34 rotor under forward flight conditions with available experimental data. In addition, the steady and unsteady lifting cases were calculated for blades with three different tips in order to investigate the aerodynamic effects of tip shapes. During all the simulations in this study, the rotor is not computationally trimmed.

### A. Caradonna and Tung Model Rotor in Hover

The Caradonna and Tung model rotor has two blades, each one with an aspect ratio of 6.0, which are untwisted and untapered, and have a NACA-0012 airfoil section. The operation condition is $\mu = 0$, $M_{\text{tip}} = 0.877$, and $\theta_0 = 8$ deg, respectively.

Figures 3 and 4 show the predicted pressure distributions along the airfoil section at a radial position of $r/R = 0.89$, and the lift distributions along the blade, respectively. For comparison proposes, the experimental data,[15] and the results calculated by a second-order center difference scheme and a high-order upwind scheme without free wake were also superimposed on these plots. It is clear from the comparisons in the figures that the results predicted using the proposed hybrid method correlate better with the experimental data, when compared with the results predicted with either the second-order center difference scheme or the high-order upwind scheme without the free wake model.

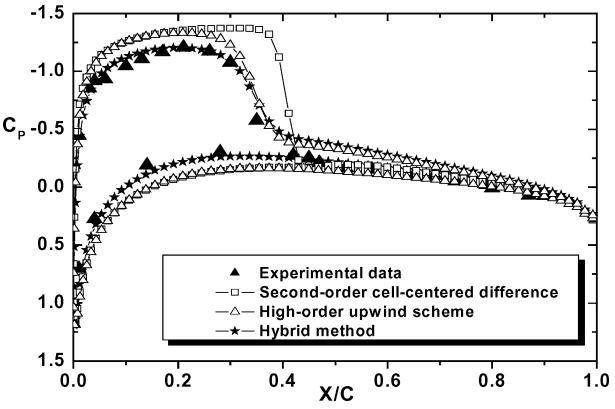


**Fig. 3 Surface pressure distribution on a lifting Caradonna and Tung model rotor blade ($r/R = 0.89$, $M_{\text{tip}} = 0.877$, $\theta_0 = 8$ deg).**

Figures 5a and 5b show the predicted trajectories of the tip vortex in the radial and vertical directions, respectively, along with comparisons with the experimental data from Ref. 15. The operating conditions of the rotor are $M_{\text{tip}} = 0.877$ and $\theta_0 = 8$ deg. From the comparisons of the radial contraction as shown in Fig. 5a, it can be seen that the simulation results using a second-order center difference scheme correlate well with the experimental data for a wake age only up to 140 deg. After this point, the vortex trajectories predicted using the scheme are less contracted toward the center of rotation than those of experimental data, which may be due to the simulated vortical wake dissipation resulting from truncation error and artificial viscosity in the second-order center difference scheme. However, the trajectories simulated using the present hybrid method

correlate well with the experimental data for a wake age up to 360 deg as seen in the figure. Similarly, from the comparisons of the vertical displacement of the tip vortex in Fig. 5b, it can be seen that the vertical displacement of the tip vortex simulated using the proposed hybrid method demonstrates good agreement with the experimental data for the wake age up to 360 deg.

### B. UH-60A Rotor in Hover

Simulations are run for the flowfield of a four-bladed UH-60A helicopter rotor. The rotor blade has a rearward sweep of 20 deg starting from 93% radius, and an aspect ratio of 15.3 and a negative maximum twist of 13 deg. The blade is made up of two airfoil sections, an SC1095 section as its main airfoil and an SC1095R8 section in the midspan.[16]

Figure 6 shows the surface pressure distributions at two different radial stations along the rotor blade, which operates at $M_{\text{tip}} = 0.628$ and $\theta_0 = 10$ deg, simulated using the proposed hybrid method, including comparisons with the corresponding test data.[16] Again, for comparison purposes, the simulation results without any rotor wake model using a second-order center difference scheme are superimposed on the plot. From the comparisons, it can be clearly seen that the simulated pressure distributions on the rotor blade, predicted with the proposed hybrid method, correlate better with the experimental data than those calculated using the second-order center difference scheme without wake model. This improved correlation with test data is due to the effective reduction of false dissipation of rotor wake in the current hybrid method, when compared to the center difference method without wake model.

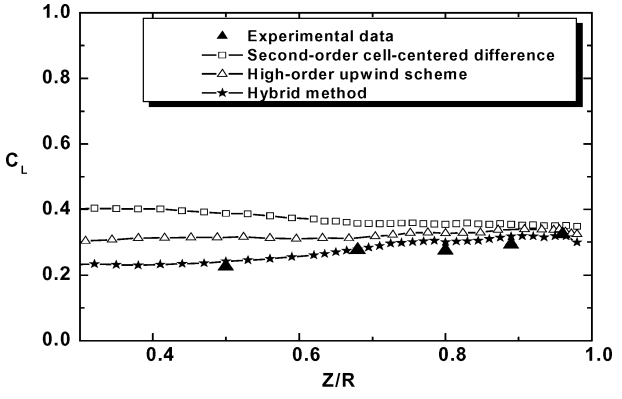


**Fig. 4 Sectional lift coefficients on a Caradonna and Tung model rotor blade ($M_{\text{tip}} = 0.877$, $\theta_0 = 8$ deg).**

### C. AH-1G Rotor in Forward Flight

The present hybrid solver is also used to simulate the flowfield around a two-bladed AH-1G rotor under the forward flight condition. The rotor operates at $\mu = 0.19$, $M_{\text{tip}} = 0.65$, $\theta_0 = 6.0$ deg, $A_1 = -5.5$ deg, $B_1 = 1.7$ deg, $a_{1s} = -0.15$ deg, and $b_{1s} = 2.13$ deg, respectively. The rotor blade has an aspect ratio of 9.8 and a linear twist of $-10$ deg from root to tip.

Figure 7 is the surface pressure distributions along the airfoil surface on both the advancing and retreating side predicted using the present hybrid method, together with comparisons with the test data[17] and Yang's calculated results.[6] The results predicted using a second-order cell-centered difference scheme and a high-order upwind method are also superimposed on the figure. As shown in Fig. 7, the pressure distributions predicted using the present hybrid method correlate well with test data on both the advancing and retreating sides, when compared to the results predicted with either a second-order cell-centered difference scheme or a high-order upwind scheme, which indicates the potential of the present method in capturing the flowfield around the rotor blades in forward flight.

### D. H-34 Rotor in Forward Flight

The proposed hybrid solver is also applied to simulate the flow field around a H-34 helicopter rotor in forward flight. The simulation results are compared with the corresponding flight test data.[18] The rotor considered here has four blades with a NACA 0012 airfoil, which have a linear twist of $-8$ deg and an aspect ratio of 20.48. The

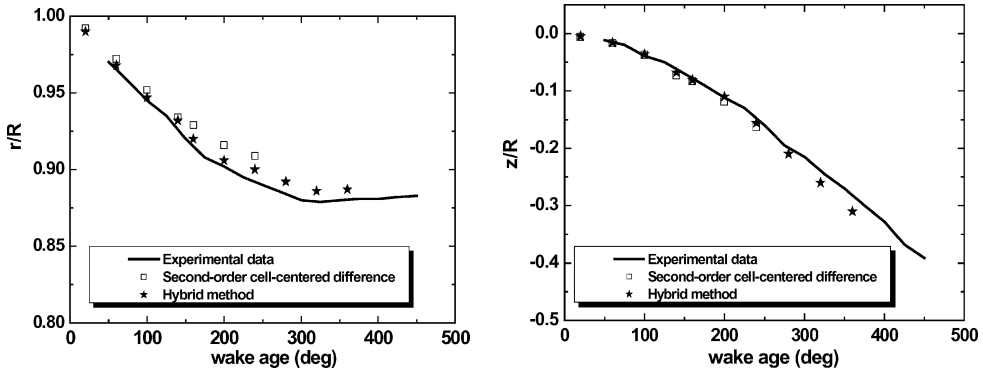


**a) Radial location** **b) Vertical location**

**Fig. 5 Tip vortex location of the Caradonna and Tung model rotor ($M_{\text{tip}} = 0.877$, $\theta_0 = 8$ deg).**

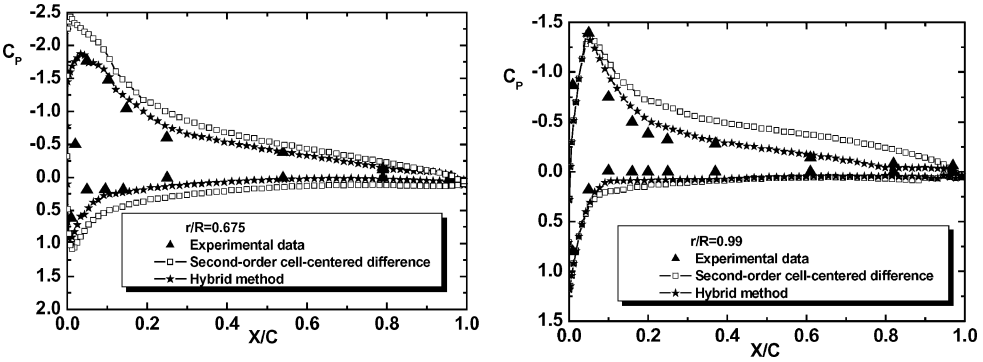


**Fig. 6 Surface pressure distributions on a UH-60A rotor blade ($M_{\text{tip}} = 0.628$, $\theta_0 = 10$ deg).**

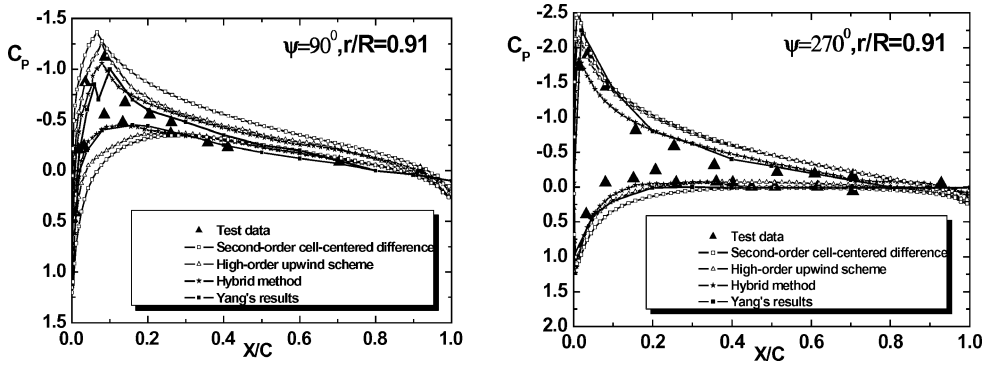


**Fig. 7 Surface pressure distributions for the AH-1G rotor in forward flight ($\mu = 0.19$ and $M_{\text{tip}} = 0.65$).**

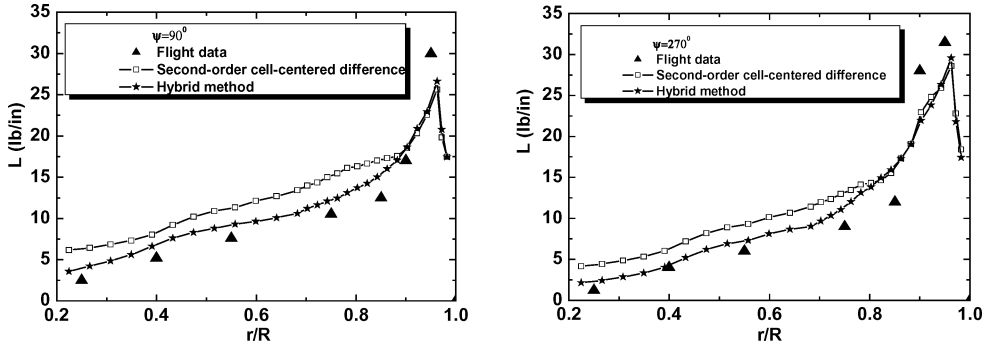


**Fig. 8 Spanwise lift distribution along the blade on advancing and retreating sides in forward flight ($\mu = 0.064$ and $M_{\text{tip}} = 0.544$).**

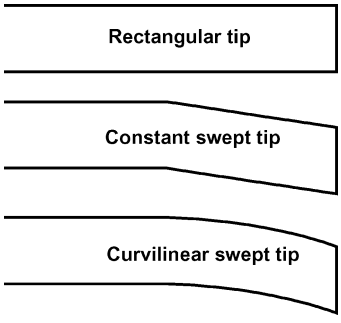


**Fig. 9 Planforms of three different blade tips.**

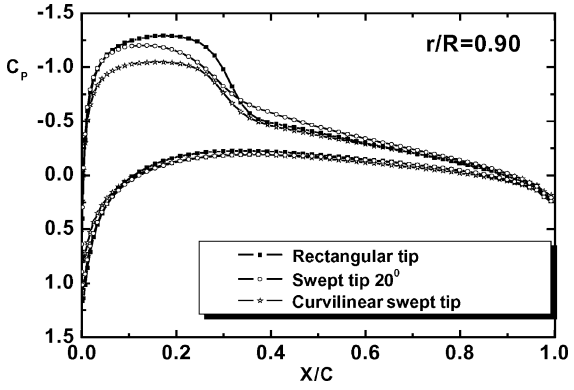


**Fig. 10 Surface pressure distributions on a lifting rotor blade with different tips ($\mu = 0$, $M_{\text{tip}} = 0.85$, and $\theta_0 = 8$ deg).**

rotor operates at $M_{\text{tip}} = 0.544$ and $\mu = 0.064$. The blade feathering and flapping motion coefficients for this case are $\theta_0 = 12.3$ deg, $A_1 = -2.2$ deg, $B_1 = 0.35$ deg, and $a_0 = 3.6$ deg, $a_{1s} = -0.01$ deg, $b_{1s} = 0.34$ deg, respectively.

The spanwise lift distributions along the rotor blade at two azimuthal stations ($\psi = 90$ deg and $\psi = 270$ deg) predicted with the proposed hybrid method are shown in Fig. 8, including comparisons with the results predicted with a second-order center difference scheme. As clearly shown in Fig. 8, the lift distribution along the rotor blade predicted with the hybrid method correlates well with the test data, when compared to the results by the second-order center difference scheme. Similarly to the hover case, the improvements is obviously because the hybrid method with a free wake analysis effectively reduces the false dissipation of rotor wake. However, it can be also seen from the figure that at the tip regions, where the measured lift distribution increases rapidly, the correlation is not very good. To capture the flowfield at the tip regions where the flow characteristics change rapidly, more grid points should be included.

### E. Rotors with Different Tip Shapes in Hover and Forward Flight

The proposed hybrid method was also used to calculate the steady and unsteady lifts for a model rotor. The rotor has two blades with an aspect ratio of 7.0, which are untwisted and untapered, and have the NACA-0012 airfoil section with three different tips, the rectangular tip, the constant swept tip, with the swept position of $r/R = 0.86$, and the curvilinear swept tip, which are shown in Fig. 9, in order to compare the effects of tip shapes. In Fig. 9, the model rotors with three different blade tips have the same solidity.

Figure 10 gives the calculated surface pressure distributions at $r = 0.9R$ in hover for the three blade-tip planforms. The operating conditions of the rotor are $M_{\text{tip}} = 0.85$ and $\theta_0 = 8$ deg. As clearly demonstrated in the results, the shock strength on the constant swept tip blade is weaker than that of the rectangular tip case, but stronger than that of the curvilinear swept tip case.

Figure 11 shows the pressure distributions on the airfoil upper surface along azimuth for $\mu = 0.3$, $M_{\text{tip}} = 0.6$, $\theta(t) = 9$ deg, and $\beta(t) = 0$ deg. It provides a complete picture of the supercritical flow areas over the tip region of three blades. On the rotor disk, the onset and development of supercritical flow over the advancing tip are appreciably delayed by the incorporation of tip sweepback, and the suppression of supercritical flow obtained with the curvilinear swept tip is more evident than with the constant swept tip. These

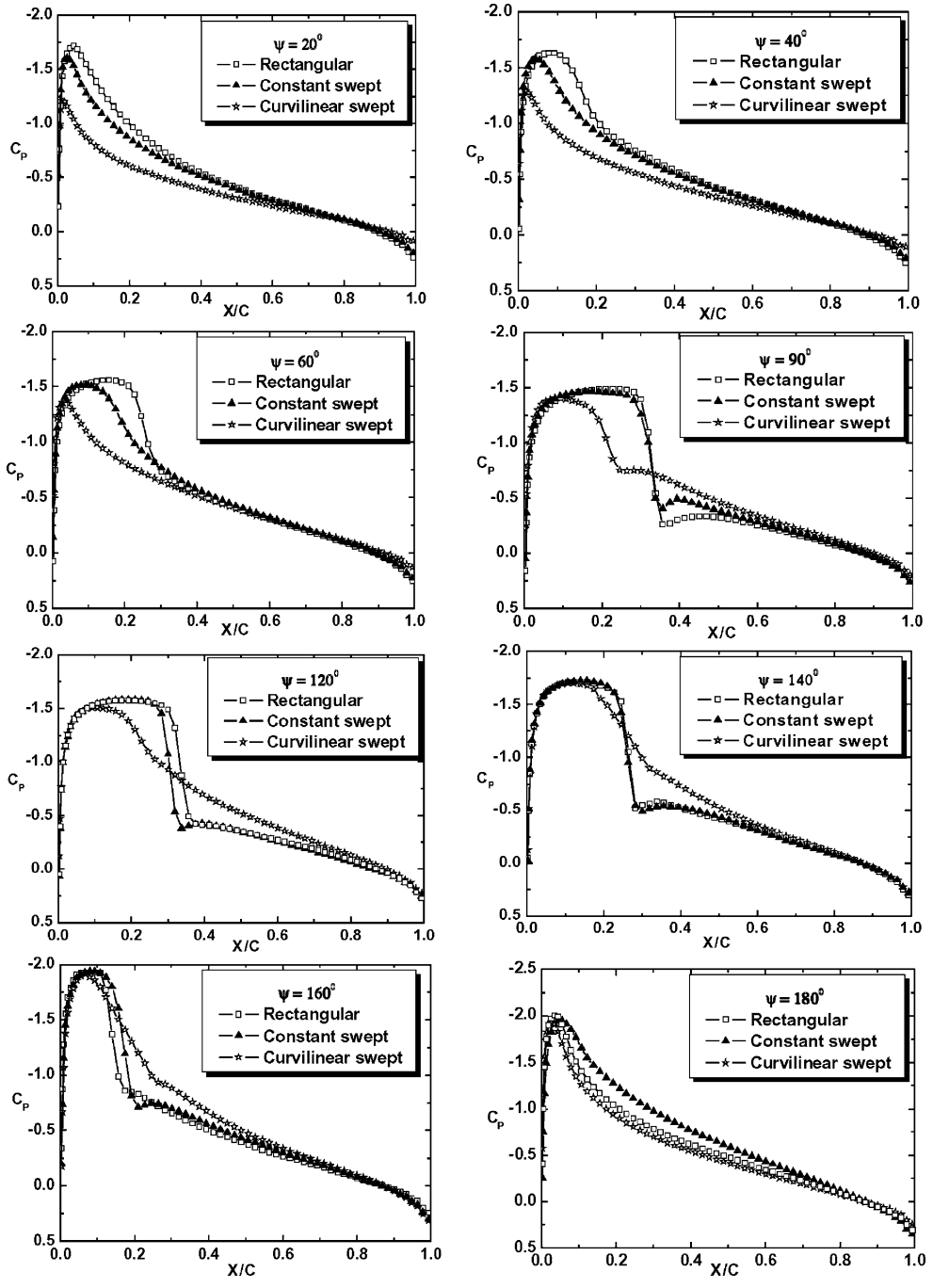


**Fig. 11 Surface pressure distributions showing shock position on airfoil upper surface ($\mu = 0.3$, $M_{\text{tip}} = 0.6$, $r/R = 0.90$, $\theta(t) = 9$ deg, and $\beta(t) = 0$ deg).**

phenomena can be explained by the fact that sweptback leads to a reduction in the component of the incident flow normal to the leading edge in some azimuth regions. As shown in Fig. 11, when supercritical flow is present, the shock wave moves forward along the blade chord as the azimuth angle increases at the advancing side. At the 140-deg azimuth position, where the component of the incident flow normal to the leading edge is higher for the swept tip than for the rectangular tip, the constant swept tip does not demonstrate to be advantageous in terms of shock strength or location, and the pressure distribution shapes are nearly the same for two tip shapes, as seen in the figure. Even at the 160-deg azimuth position, the supercritical flow is somewhat more severe on the upper surface of the constant swept blade tip when compared to the rectangular blade tip. The similar phenomena were also observed experimentally in Ref. 19. However, the curvilinear swept tip has a more favorable pressure distribution, indicative of the lower drag and smaller pitching moment, and the shock strength for this tip is weaker and the shock position is closer to the leading edge when compared to the two other blade tips.

### F. Computational Efforts

In the present study, the developed code for the proposed hybrid method was set up on a personal computer with Pentium IV 2.4G CPU. The computational resource requirements were compared between the hybrid method and the stand-alone Navier–Stokes method for a Caradonna and Tung model rotor in both hover and forward flight. The comparison results are given in Table 1, and the two methods are performed in the same embedded grids. For the Navier–Stokes calculations in hover, the converged solution was achieved in approximately 550 time steps for a Courant number of 3. The corresponding CPU time is about 9.5 h on the personal computer. For the same case considered, the computer time is about 6.2 h using the proposed hybrid method, which means that approximately 35%

**Table 1 Comparison of the CPU time (h) between the two solvers**

| | Solver | |
|---|---|---|
| Calculation case | Hybrid method | Stand-alone Navier–Stokes |
| A typical hover case | 6.2 | 9.5 |
| A typical forward-flight case | 38 | 62 |

CPU time reduction is achieved. In the comparison computations, when the number of normal grids of the C-H type rotor grid is decreased by 20%, the CPU times consumed using the hybrid method and the stand-alone Navier–Stokes calculations are about 5.6 and 9.8 h, respectively, which demonstrates approximately 43% CPU time reduction with the present method.

A typical calculation for the forward flight condition requires approximately 62 h of CPU time, which needs about three rotor revolutions and about 35 iterations for a step size of 5 deg in the azimuth direction to obtain a converged solution by the stand-alone Navier–Stokes calculations. But using the hybrid method, it costs about 38 h of CPU time, which indicates an approximately 39% CPU time reduction.

## VI. Conclusions

A new hybrid Navier–Stokes/full-potential/free wake solver was developed in this work for the prediction of the flowfield around helicopter rotors in both hover and forward flight. The developed solver was validated through comparing surface pressure distributions with available experimental data or the simulation results by other researchers in the literatures. The solver was also applied to investigate the effects of different blade tips on rotor flow. The following conclusions can be drawn:

1) The proposed hybrid method is not only capable of capturing well the characteristics of flow over the helicopter rotor in hover and forward flight, which is due to the reason that the free wake model can account for the rotor wake more reasonably, but also to lead to about 40% CPU time reduction, when compared to the stand-alone Navier–Stokes calculations.

2) A combination of the moving embedded grid methodology and the pseudo-searching scheme of donor elements (PSSDE) can account for the rigid blade motions in rotation, flapping, and feathering and was shown to be effective and robust in searching the corresponding donor elements and getting the interpolated data for the information communication among the full-potential zone, Navier–Stokes zone and free wake.

3) The combination of the third-order upwind scheme (MUSCL) and flux-difference splitting scheme can effectively reduce the false dissipation of the rotor wake vorticity without introducing artificial viscosity. The present finite-volume approximation and dual-time method can be used to predict the three-dimensional of complicated unsteady flowfield for helicopter rotors and run on typical personal computers.

4) The simulated steady and unsteady lifting results in this paper demonstrate the effectiveness of the constant swept tip in alleviating the adverse high-Mach-number effects near the tip on the advancing blade, except in some azimuthal region, and the curvilinear swept tip is more favorable than a constant swept tip for suppressing the supercritical flow when compared to the same rotor with rectangular blade tip. This improvement is mainly due to the decrease of the transonic flow intensity on the swept tips, especially on the advancing side in forward flight.

## References

[1]Conlisk, A. T., "Modern Helicopter Rotor Aerodynamics," *Progress in Aerospace Science,* Vol. 37, No. 5, 2001, pp. 419–475.

[2]Duque, E., Biswas, R., and Strawn, R., "A Solution-Adaptive Structured/Unstructured Overset Grid Flow Solver with Applications to Helicopter Rotor Flows," AIAA Paper 95-1766, 1995.

[3]Strawn, R. C., and Barth, T. J., "A Finite-Volume Euler Solver for Computing Rotary-Wing Aerodynamics on Unstructured Meshes," *Journal of the American Helicopter Society,* Vol. 38, No. 2, 1993, pp. 61–67.

[4]Hanriharan, N., and Sankar, L. N., "First-Principles Based High Order Methodologies for Rotorcraft Flowfield Studies," *Proceedings of 55th Annual Forum of AHS*, Vol. 1, Montreal, 1999, pp. 1921–1933.

[5]Berkman, M. E., Sankar, L. N., Berezin, C. R., and Torok, M. S., "Navier–Stokes/Full Potential/Free-Wake Method for Rotor Flows," *Journal of Aircraft*, Vol. 34, No. 5, 1997, pp. 635–640.

[6]Yang, Z., Sankar, L. N., Smith, M. J., and Bauchau, O., "Recent Improvements to a Hybrid Method for Rotors in Forward Flight," *Journal of Aircraft*, Vol. 39, No. 5, 2002, pp. 804–812.

[7]Hariharan, N., and Sankar, L. N., "Application of ENO Schemes to Rotary Flow Field," AIAA Paper 95-1892, 1995.

[8]Zhao, Q. J., and Xu, G. H., "Grid Generation Technique for Helicopter Rotor CFD Including Blade Motions," *Journal of Nanjing University of Aeronautics and Astronautics*, Vol. 36, No. 3, 2004, pp. 288–293. [In Chinese]

[9]Jameson, A., Schmidt, W., and Turkel, E., "Numerical Solution of the Euler Equations by Finite Volume Methods Using Runge–Kutta Time Stepping Scheme," AIAA Paper 81-1259, 1981.

[10]Roe, P. L., "Approximate Riemann Solver, Parameter Vectors and Difference Schemes," *Journal of Computational Physics*, Vol. 43, No. 2, 1981, pp. 357–372.

[11]Harten, A., and Hyman, J. M., "Self Adjusting Grid Methods for One-Dimensional Hyperbolic Conservation Laws," *Journal of Computational Physics*, Vol. 50, No. 2, 1983, pp. 235–269.

[12]Xu, G. H., and Wang, S. C., "An Analytical Method for Predicting Aerodynamic Characteristics of the Rotor with a Swept Tip," *Acta Aerodynamica Sinica*, Vol. 17, No. 3, 1999, pp. 356–361. [In Chinese]

[13]Bagai, A., and Leishman, J. G., "Rotor Free-Wake Modeling Using a Pseudo-Implicit Technique-Including Comparisons with Experimental Data," *Journal of the American Helicopter Society*, Vol. 40, No. 3, 1995, pp. 29–41.

[14]Mahendra, J. B., and Leishman, J. G., "On the Relationship between Blade Circulation and Tip Vortex Characteristics," *Proceedings of 54th Annual Forum of AHS*, Vol. 1, Washington, DC, 1998, pp. 557–575.

[15]Caradonna, F. X., and Tung, C., "Experimental and Analytical Studies of a Model Helicopter Rotor in Hover," *Vertica*, Vol. 5, No. 2, 1981, pp. 149–161.

[16]Lorber, P. F., Stauter, R. C., and Landgrebe, A. J., "A Comprehensive Hover Test of the Airloads and Airflow of an Extensively Instrumented Model Helicopter Rotor," *Proceedings of 45th Annual Forum of AHS*, Boston, 1989, pp. 281–296.

[17]Cross, J. L., and Watts, M. E., "Tip Aerodynamics and Acoustics Test: A Report and Data Survey," NASA RP-1179, NASA Ames Research Center, Dec. 1988.

[18]Scheiman, J., "A Tabulation of Helicopter Rotor-Blade Differential Pressures, Stresses and Motions as Measured in Flight," NASA TM X-952, March 1964.

[19]Wilby, P. G., and Philippe, J. J., "An Investigation of the Aerodynamics of an RAE Swept Tip Using a Model Rotor," *Proceedings of 39th Annual Forum of AHS*, St. Louis, MS, 1983, pp. 724–740.